

SCIENTIFIC REPORTS

OPEN

Graphene-Wrapped Anatase TiO₂ Nanofibers as High-Rate and Long-Cycle-Life Anode Material for Sodium Ion Batteries

Received: 18 March 2015

Accepted: 06 August 2015

Published: 10 September 2015

Yeolmae Yeo¹, Ji-Won Jung¹, Kyusung Park² & Il-Doo Kim¹

Anatase TiO₂ has been suggested as a potential sodium anode material, but the low electrical conductivity of TiO₂ often limits the rate capability, resulting in poor electrochemical properties. To address this limitation, we propose graphene-wrapped anatase TiO₂ nanofibers (rGO@TiO₂ NFs) through an effective wrapping of reduced graphene oxide (rGO) sheets on electrospun TiO₂ NFs. To provide strong electrostatic interaction between the graphene oxide (GO) sheets and the TiO₂ NFs, poly(allylamine hydrochloride) (PAH) was used to induce a positively charged TiO₂ surface by the immobilization of the -NH₃⁺ group and to promote bonding with the negatively charged carboxylic acid (-COO⁻) and hydroxyl (-OH) groups on the GO. A sodium anode electrode using rGO@TiO₂ NFs exhibited a significantly improved initial capacity of 217 mAh g⁻¹, high capacity retention (85% after 200 cycles at 0.2C), and a high average Coulombic efficiency (99.7% from the second cycle to the 200th cycle), even at a 5C rate, compared to those of pristine TiO₂ NFs. The improved electrochemical performances stem from highly conductive properties of the reduced GO which is effectively anchored to the TiO₂ NFs.

Lithium-ion batteries (LIBs) have been widely used as power sources for portable electronic devices and hybrid electric vehicles. However, the growing usage and application of LIBs bring a fundamental question as to whether lithium resources on earth can cover future industrial demands. For this reason, many researchers have studied other energy-storage devices beyond LIBs. The sodium-ion batteries (NIBs) are a promising candidate because it is similar to the conventional LIB system in terms of the charge/discharge mechanism and the cell configuration. A number of notable studies of NIB have been conducted recently in search of cost-effective, high-capacity, and structurally/electrochemically stable sodium-ion electrode materials¹⁻⁴.

Recently, tin (Sn)^{5,6}, antimony (Sb)⁷ and red phosphorus (red P)^{8,9} were reported as promising sodium-ion anode materials¹⁰. They have high theoretical specific capacities of 847 mAh g⁻¹ for Na₁₅Sn₄¹¹, 660 mAh g⁻¹ for Na₃Sb¹¹ and 2596 mAh g⁻¹ for Na₃P⁸. However, these high-capacity anode materials undergo large volume changes during cycling, which can generate pulverization or cracks, eventually leading to cell failure. For example, after sodiation, the theoretical volumetric expansions of Na₁₅Sn₄⁶, Na₃Sb¹¹, and Na₃P⁸ were approximately 420%, 390% and 308%, respectively. As experienced in the LIB system, the volumetric expansion problem is difficult to solve because it stems from the intrinsic properties of the materials, which are related to structural changes during sodiation. Consequently, alternative anode materials which undergo minimal volume changes should be found for the practical application of NIBs.

¹Department of Materials Science and Engineering, Korea Advanced Institute of Science and Technology (KAIST), 291 Daehak-ro, Yuseong-gu, Daejeon 305-701, Republic of Korea. ²Texas Materials Institute, The University of Texas at Austin, Austin, Texas 78712, United States. Correspondence and requests for materials should be addressed to I.-D.K. (email: idkim@kaist.ac.kr)

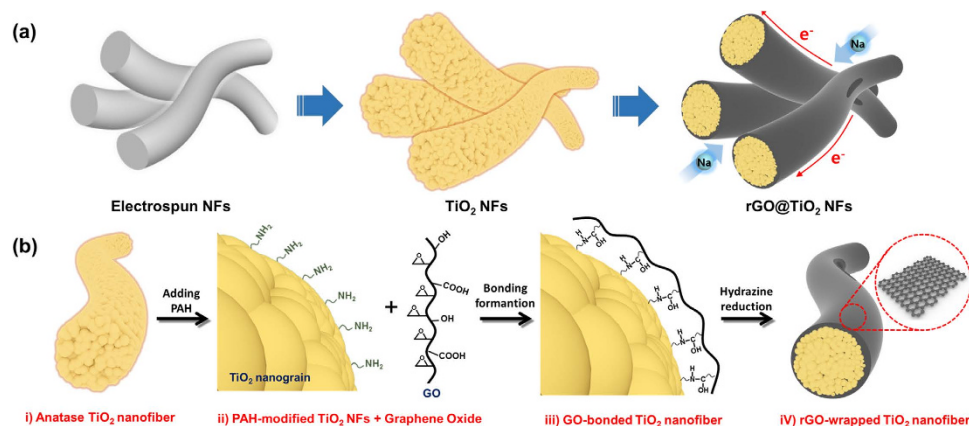


Figure 1. Synthesis of graphene-TiO₂ NFs. (a) products at each synthetic step: as-spun NFs by electrospinning, anatase TiO₂ NFs after calcination at 500 °C for 1 h, and rGO@TiO₂ NFs by graphene-wrapping. (b) graphene-wrapping mechanism: i) the surfaces of the as-prepared anatase TiO₂ NFs are functionalized to amine groups with an aqueous PAH solution (PAH-modified TiO₂ NFs), ii) the GO-TiO₂ NF composite solution was formulated by adding a GO solution to a PAH-TiO₂ NF solution, iii) Strong bonding formation between GO and TiO₂ NFs through cross-linking, and iv) GO reduced by hydrazine to obtain the rGO@TiO₂ NF solution. Proper centrifugation and drying followed after each step. This figure was drawn by one of co-authors.

In this regard, TiO₂ is a particularly interesting anode material. Xu *et al.* first reported anatase TiO₂ (hereafter, TiO₂) for a sodium-ion battery with a stable cycle life of 100 cycles¹². After this study, TiO₂ received much attention as a promising sodium-ion anode material¹³. In-depth studies of the electrochemical reaction mechanism between the Na⁺ and TiO₂ have also been conducted^{14,15}. It is believed that TiO₂ stores Na⁺ below 0.8 V through the Ti⁴⁺/3⁺ redox reaction, which is based on Na⁺ insertion in the host structure. Then, the metastable sodium titanate phase is converted into metallic titanium, sodium superoxide and an amorphous sodium titanate phase at 0.3 V vs Na/Na⁺ during cycling. One major concern about TiO₂ is its low electrical conductivity owing to its high bandgap of ~3.2 eV, which gives rise to the insulating nature of intrinsic TiO₂ without a dopant¹⁶. In order to improve the electrical transport characteristics of TiO₂, several studies have been performed to achieve nanostructural TiO₂ (i.e., nanoparticles, nanorod, nanotube)^{17–19} with advanced carbonaceous materials such as carbon nanotubes (CNTs)²⁰ or graphene²¹. A carbon-modified TiO₂ composite showed a noticeable improvement in its electrochemical performance, but it still had problems such as a high cost and low productivity due to its complex manufacturing process.

In particular, for LIB applications, graphene-TiO₂ composite structures, including those with TiO₂ particles decorated onto the surface of graphene^{22,23}, stacked TiO₂ and graphene layers²⁴, structures with physically mixed TiO₂ particles and graphene²⁵, and those with TiO₂ particles wrapped with graphene²⁶ have been widely studied. However, a simple mixing route between carbon/graphene and zero-dimensional (0D) oxide nanoparticles often requires large amounts of carbon/graphene. Severe aggregation of the oxide nanoparticles or the graphene itself is easily observed during the mixing process. On the other hand, well-interconnected one-dimensional (1D) nanostructures can greatly improve the electrochemical kinetics owing to a reduced diffusion length to the fiber core ($t = L^2/D$; t : reaction time, L : ion diffusion length, D : diffusion coefficient)²⁷. For such a 1D nanostructure, intriguingly, the graphene-wrapping route offers significantly improved cycle performance and rate capability with a small amount of graphene and without the aggregation of the graphene sheets. In this study, we propose graphene-wrapped 1D TiO₂ nanofibers (hereafter, TiO₂ NFs) for the first time as a high-rate and long-cycling anode material for sodium-ion batteries. In this study, 1D TiO₂ NFs were prepared via an electrospinning method, and poly (allylamine hydrochloride) (PAH) was used as a surface modifier to induce a positively charged TiO₂ surface, i.e., -NH₃⁺-grafted TiO₂ NFs²⁸. Then, the graphene-wrapping process was done to obtain graphene-wrapped TiO₂ NFs. The electrochemical sodiation/desodiation properties of the graphene-wrapped TiO₂ NFs and their reaction mechanism are discussed.

Results

Schematic illustration of the electrospinning and graphene-wrapping process. Figure 1 shows the processing steps for the synthesis of the reduced graphene-oxide-wrapped TiO₂ NFs (hereafter, rGO@TiO₂ NFs). The rGO@TiO₂ NFs were obtained by several synthetic steps, and the products in each step are shown in Fig. 1a. First, as-spun Ti precursor/polymer composite NFs were obtained via an electrospinning method. After high-temperature calcination, the TiO₂ NFs were formed by the thermal decomposition of the matrix polymer and the crystallization of the TiO₂ particles composing

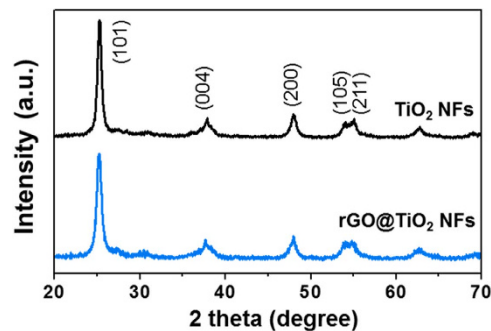


Figure 2. X-ray diffraction patterns of TiO_2 NFs and rGO@TiO_2 NFs.

the NFs. With regard to the graphene-wrapping method, its mechanism is illustrated in Fig. 1b. In order to provide strong electrostatic interaction between the negatively charged graphene oxide (GO) and the as-prepared TiO_2 NFs above, (i) we grafted the surfaces of the TiO_2 NFs by using poly (allylamine hydrochloride) (PAH). TiO_2 NFs were positively charged by $-\text{NH}_3^+$ in the solution; (ii) Subsequently, GO sheets were added to the TiO_2 NF-dispersed solution, and the solution was mechanically agitated to ensure homogeneous mixing. GO sheets have sufficient functional groups such as carboxylic acid ($-\text{COOH}$) and hydroxyl ($-\text{OH}$) groups, which induce surface-negative charges ($-\text{COO}^-$ and $-\text{O}^-$) in the solution. Then, the positively charged TiO_2 NFs and the negatively charged GO are self-assembled; (iii) Crosslinking between GO and PAH arises due to ring-opening of the epoxy groups of GO as well as partial contribution of the carboxylic group, originated from the nucleophile reaction of the unpaired electrons of the amine groups²⁸; (iv) Finally, hydrazine was added to the mixed solution including the GO and PAH-modified TiO_2 NFs to transform the GO sheets into reduced GO (rGO) sheets. This graphene-wrapping mechanism was discussed in our previous report²⁹. As part of the processes above, proper centrifuging and drying were conducted.

Characteristics of TiO_2 NFs and rGO@TiO_2 NFs. Figure 2 shows the X-ray diffraction (XRD) patterns of the TiO_2 NFs and the rGO@TiO_2 NFs. The XRD patterns of both samples confirm that they have the original anatase TiO_2 structure (space group $I4_1/amd$, JCPDS PDF#21–1272). The main peak of the anatase TiO_2 at 25.2° indicates the crystal lattice plane (101), and other strong peaks at 37.8° , 48° , 54.8° , and 55° present the (004), (200), (105) and (211) planes, respectively. Moreover, it is important to note that the graphene-wrapping process did not affect the crystal structure of the TiO_2 . Using the Scherrer equation, $d = \frac{0.94\lambda}{w \times \cos \theta}$ we estimated the mean crystallite size of the nanoparticles comprising the polycrystalline TiO_2 NFs. In equation 1, d is the mean grain size, λ is the wavelength of the Cu K_α radiation (0.154 nm), θ is the Bragg angle considered, and w is the line width at half-maximum intensity on the 2θ scale, in radians. From this calculation, we estimated the average crystallite size of the anatase TiO_2 to be 15.5 nm.

The morphological features of the TiO_2 NFs and rGO@TiO_2 NFs were characterized by scanning electron microscopy (SEM) and transmission electron microscopy (TEM), respectively. As shown in the SEM images in Fig. 3a,b, calcined TiO_2 NFs with a diameter of approximately 200–300 nm exhibited a wrinkled surface and a straight line shape. The high-resolution TEM (HRTEM) image of the calcined TiO_2 NFs clearly confirms that the Ti precursor was crystallized into polycrystalline TiO_2 , which is composed of small nanoparticles (Fig. 3c,d). The lattice fringes of the TiO_2 (3.52 Å) NF correspond to the TiO_2 (101) plane (JCPDS PDF#21–1272). Figure 3e,f depict SEM images of the rGO@TiO_2 NFs. The rGO sheets cover all the surfaces of the TiO_2 NFs well and effectively interconnect the TiO_2 NFs to each other. Figure 3g exhibits a TEM image of the edge structure of the rGO@TiO_2 NFs. We note the HRTEM image in Fig. 3h, which is a highly magnified image of the yellow frame in Fig. 3g and which reveals that the thickness of the rGO sheets is approximately 3 nm.

To provide further investigation, we conducted Raman and FT-IR analyses of both the TiO_2 NFs and rGO@TiO_2 NFs. The Raman spectra of the TiO_2 NFs exhibit peaks which are located at approximately 145, 398, 520 and 640 cm^{-1} (Fig. 4). These peaks correspond to the lattice vibrational model of the $E_g(1)$, $B_{1g}(1)$, $B_{1g}(2) + A_{1g}$ and $E_g(3)$ bands of the anatase TiO_2 , respectively³⁰. The Raman spectra of the rGO@TiO_2 NFs equally contain the $E_g(1)$, $B_{1g}(1)$, $B_{1g}(2) + A_{1g}$ and $E_g(3)$ bands of the anatase TiO_2 , which also confirms that the graphene-wrapping process does not cause any local structure changes. Likewise, the rGO@TiO_2 NFs show two peaks of rGO at 1349 and 1605 cm^{-1} . These two peaks denote the general G and D bands of rGO, respectively³¹. The Raman analysis clearly verified that the structural properties of the TiO_2 NFs, which were well covered by rGO, did not change after the graphene-wrapping process.

Figure 5 presents the Fourier-transformed infrared (FT-IR) spectra of the TiO_2 NFs, the rGO@TiO_2 NFs, and GO in H_2O . The GO in H_2O was measured in the attenuated total reflection (ATR)

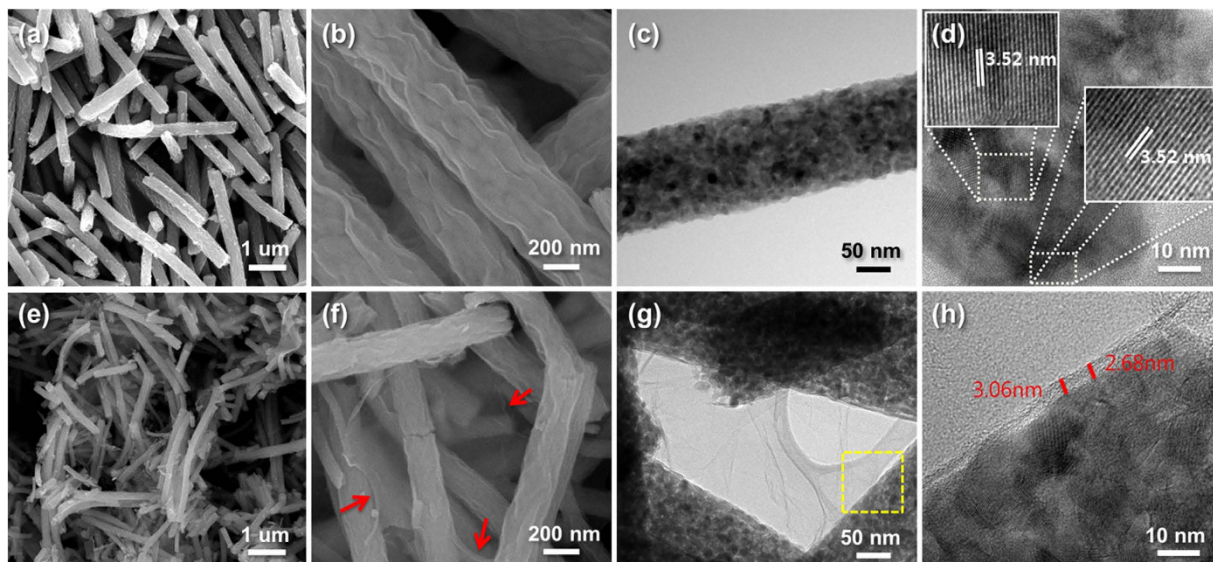


Figure 3. (a–b) SEM and (c–d) TEM images of TiO_2 NFs; (e–f) SEM and (g–h) TEM images of rGO@TiO_2 NFs. (h) shows an HRTEM image of the yellow frame in (g). Lattice of the anatase TiO_2 (inset images); the graphene connection (red arrows) and thickness of the graphene wrapping (red lines) are well shown.

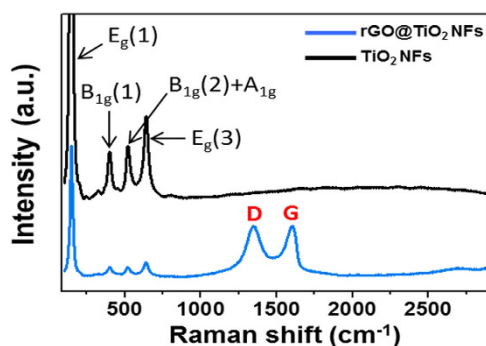


Figure 4. Raman spectra of TiO_2 NFs and rGO@TiO_2 NFs.

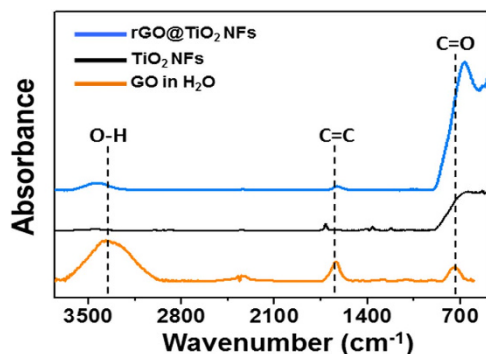


Figure 5. FT-IR spectra of TiO_2 NFs, rGO@TiO_2 NFs and the GO solution in H_2O .

mode. Both the TiO_2 NFs and rGO@TiO_2 NFs showed Ti-O and Ti-O-Ti vibrations at $500\text{--}700\text{ cm}^{-1}$ ³², which provides evidence of the structural identity of these two materials. Furthermore, several bands located at a similar wavenumber in both the rGO@TiO_2 NFs and the GO in H_2O revealed that the graphene-wrapping process was successful. The broad band on the rGO@TiO_2 NFs overlaps with the C=O stretch of the carbonyl groups at the edges of GO at 740 cm^{-1} . Moreover, the C=C stretch at

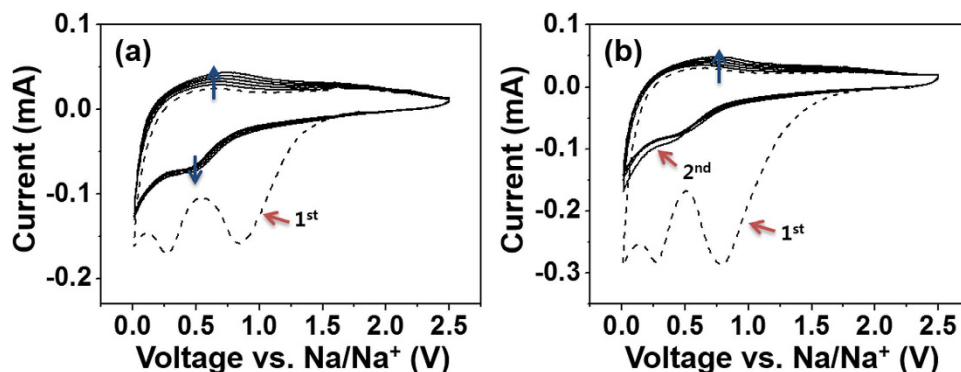


Figure 6. Cyclic voltammetry of (a) TiO₂ NFs and (b) rGO@TiO₂ NFs tested at a scan rate of 0.5 mV s⁻¹ for six cycles.

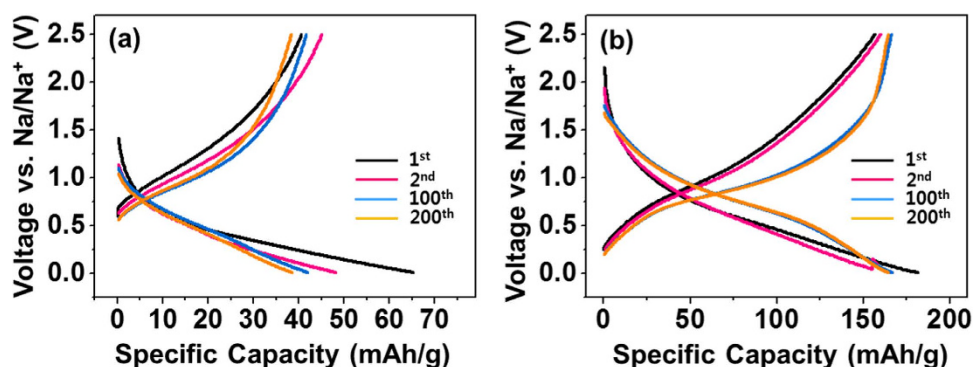


Figure 7. Charge and discharge curves of (a) TiO₂ NFs and (b) rGO@TiO₂ NFs at a 1 C (335 mA g⁻¹) rate.

1630 cm⁻¹ and the bending vibration O-H stretch at 3100–3500 cm⁻¹ are apparent in both the rGO@TiO₂ NFs and the GO in H₂O³¹.

Electrochemical reaction with Na⁺. Figure 6a,b show the cyclic voltammetry (CV) curves of the TiO₂ NFs and the rGO@TiO₂ NFs. A CV test was performed at a scan rate of 0.5 mV s⁻¹ at 0.01–2.5 V for six cycles.

In the first cathodic scan of the TiO₂ NFs and the rGO@TiO₂ NFs, first irreversible reduction peaks at approximately 0.84 V are assigned to the formation of a solid electrolyte interface (SEI), and the second reduction peaks and the third peaks near 0.26 V and 0.02 V are attributed to sodiation and electrolyte decomposition. With subsequent cyclic sweeps, for both the TiO₂ NFs and the rGO@TiO₂ NFs, the second cathodic peaks and anodic peaks shift to higher potentials (~0.5 V and ~0.75 V). These phenomena may be caused by redox couple of Ti⁴⁺/Ti³⁺. Such results were already observed in previous study reported by Wu *et al.*³³ Upon further cathodic and anodic voltage sweeps, broad cathodic and anodic peaks near 0.5 V and 0.75 V were reversely observed in both electrodes. This result reveals that both anode materials present the same electrochemical characteristics, especially in terms of reversibility.

Discussion

Ex-situ analysis of a plausible reaction mechanism. The charge-discharge voltage curves of the electrodes using TiO₂ NFs and rGO@TiO₂ NFs at a 1 C rate (335 mAh g⁻¹) were measured after one cycle at 10 mA g⁻¹ (Supplementary Figures S1a,b). During the first cycle at 10 mA g⁻¹, the voltage curves of the two electrodes showed two plateau regions near 1.25 V and 0.2 V while discharging. These two plateau regions are ascribed to the formation of a SEI layer, which is in good agreement with the results of the initial CV curves in Fig. 6. In the 1st, 2nd, 100th, and 200th cycle during the following 1 C rate charge/discharge, most of the capacities of the TiO₂ NFs and rGO@TiO₂ NFs are below 0.6 V vs. Na/Na⁺ (Fig. 7a,b). The rGO@TiO₂ NFs showed enhanced capacity levels at all cycles and greatly improved capacity retention as compared to the TiO₂ NFs after 200 cycles; these results were 90% and 58% in the rGO@TiO₂ NFs and TiO₂ NFs, respectively. From the voltage profiles, we found that no voltage plateau appears in any of the cycles, which differs from the reported voltage profile of anatase TiO₂ for LIBs³⁴.

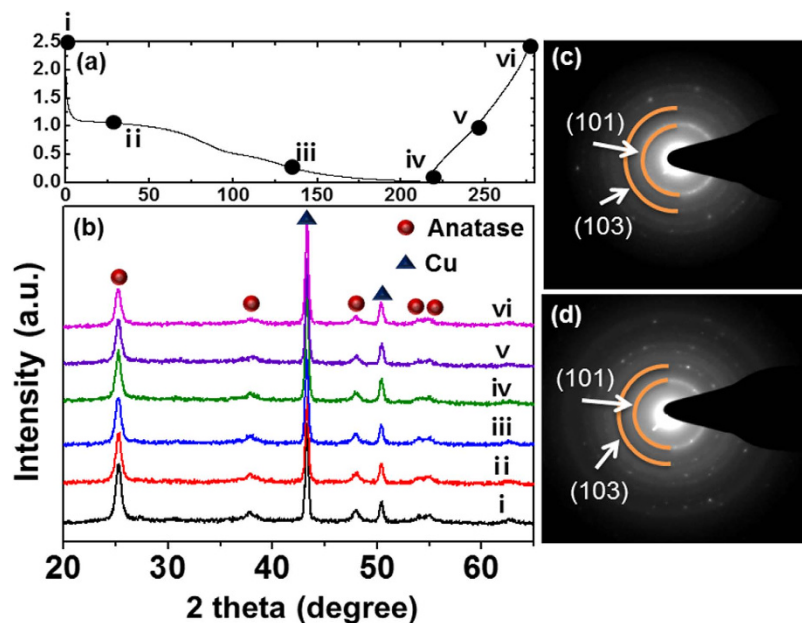
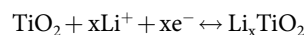


Figure 8. (a) First cycle voltage profile (X axis-specific capacity/Y axis-potential); (b) *Ex-situ* XRD data (Discharge; pristine, 1 V, 0.1 V, fully discharged. Charge; 1 V, fully charged) and SAED pattern with a TEM images in (c) fully discharged and (d) fully charged states.

In typical anatase TiO_2 , the redox potential for Li^+ insertion/deinsertion is about 1.6 V versus Li/Li^+ ; this can be written as follows:



In this regard, we studied the charge/discharge behaviors using TiO_2 NFs and rGO@TiO_2 NFs as anodes for LIBs to determine whether the smooth voltage profiles are caused by our choice of materials. The experiment using lithium metal as a counter electrode was performed at 1C rate after pre-cycling at 10 mA g^{-1} (Supplementary Figure S2). In this experiment, both the TiO_2 NFs and rGO@TiO_2 NFs exhibited a Li^+ ion insertion plateau near 1.6 V, as reported previously³⁵. This finding verifies that the reaction mechanism of TiO_2 NFs and rGO@TiO_2 NFs for lithium insertion is based on insertion, as predicted. However, in the sodium insertion case, the TiO_2 NFs and rGO@TiO_2 NFs indicate smooth charge/discharge voltage behaviors, which is fundamentally different from the case of lithium insertion. Although the effect of the particle size could cause some difference in the plateau length, generally the size effect does not eliminate this plateau. Therefore, it is important to note that the reaction mechanism of TiO_2 for NIBs may differ from that of LIBs.

To confirm the plausible reaction mechanism of anatase TiO_2 for sodium insertion/extraction, we performed *ex-situ* XRD and *ex-situ* TEM analyses. Figure 8a presents the first cycle voltage profile at a 0.2C rate. Each Roman numeral indicates the cut-off voltage for the *ex-situ* analyses. Figure 8b shows *ex-situ* XRD patterns of pristine TiO_2 NFs at 1 V, 0.1 V and 0.01 V while discharging and at 0.1 V and 2.5 V while charging. We could not find any significant structural decomposition through the *ex-situ* XRD analysis, and thus this may be interpreted as that the anatase structure was maintained during cycling. An *ex-situ* TEM analysis was performed to determine the structural stability. Figure 8c,d indicate selected-area electron diffraction (SAED) patterns in fully discharged and fully charged states, respectively. Our results rather coincide with a recent report by Kim *et al.*³⁶ Kim reported that the anatase structure is maintained during extensive cycling and suggested that the reaction mechanism is insertion through an X-ray absorption spectroscopy (XAS) analysis. This may differ from the results reported by Wu *et al.*, who claimed that the XRD reflections of the anatase phase disappear in the discharged state. Although we observed that the (004) and (200) reflections at 38° and 48° still exist after a full discharge in our case, the results in here remain controversial. Therefore, a further elaborate analysis is necessary for a precise investigation of the reaction mechanism of graphene/ TiO_2 hybrid materials.

Electrochemical performances. The galvanostatic cycles of Na-anode electrodes using TiO_2 NFs and rGO@TiO_2 NFs were tested at rates of 0.2C (67 mA g^{-1}), 1C (335 mA g^{-1}) and 5C (1.675 A g^{-1}) for 200 cycles (Fig. 9a–c). All cycle tests were performed after an initial charge/discharge process at 10 mA g^{-1} . During the galvanostatic cycles, the rGO@TiO_2 NFs maintained significantly higher specific

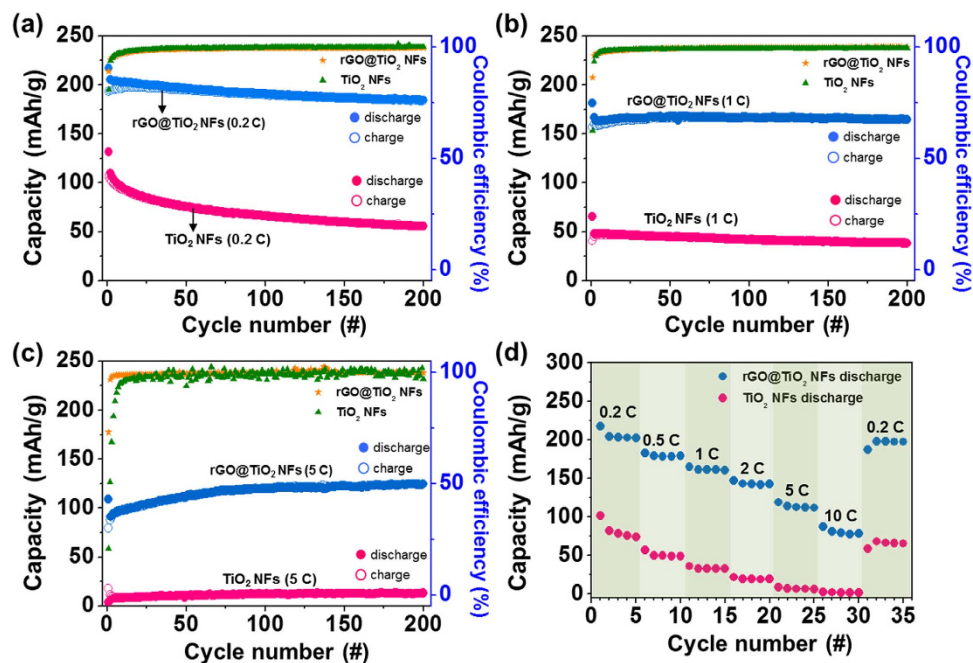


Figure 9. Charge–discharge capacity and coulombic efficiency vs. the cycle number for TiO₂ NFs and rGO@TiO₂ NFs tested (a) at a rate of 0.2C (67 mA g⁻¹), (b) at a rate of 1C (335 mA g⁻¹) and (c) at a rate of 5C (1675 mA g⁻¹). (d) Rate capabilities of TiO₂ NFs and rGO@TiO₂ NFs evaluated at various rates of 0.2C, 0.5C, 1C, 2C, 5C and 10C.

capacities than those of the TiO₂ NFs. For example, at the rates of 0.2C, 1C, and 5C, the rGO@TiO₂ NFs exhibits initial discharge capacities of 217, 165 and 124 mAh g⁻¹, respectively. Previously, Cha *et al.* showed through cyclic voltammetry that sodium ions could be stored in graphene²¹. In other words, graphene could serve as an electrochemically active material. However, in this study, we found through an elemental analysis (EA) that the detected carbon element in rGO@TiO₂ NFs was only 1.85 wt% (Supporting Information, Table S1). This negligible amount of carbon coming from graphene sheets may not appreciably contribute to the capacity of a cell. The rGO@TiO₂ NFs show very stable cycle lifetimes with high coulombic efficiency (>98%). They show high capacity retention of about 90% after 200 cycles at 1C. Moreover, at 5C, the cycling capacities of the rGO@TiO₂ NFs increase for about 70 cycles, which indicates a gradual improvement of the electrode kinetics or an increase in the active area. However, the TiO₂ NFs show a considerably low initial discharge capacity of 131 mAh g⁻¹ at 0.2C. Unfortunately, at higher rates, although this 1D nanostructured TiO₂ may make it possible effectively to transport Na⁺ with regard to the diffusion length, the original insulating property of the TiO₂ NFs markedly limited the electron transport (47 mAh g⁻¹ at a 1C rate and 12 mAh g⁻¹ at a 5C rate). For a comparison of the TiO₂ NFs and rGO@TiO₂ NFs in light of the power density, the rate performances are shown in Fig. 9d. The rGO@TiO₂ NFs exhibited high reversible capacities of 217, 182, 164, 146, 119, 87 and 197 mAh g⁻¹, while the TiO₂ NFs showed reversible capacities of 101, 56, 36, 21, 8, 2 and 68 mAh g⁻¹ at rates of 0.2C, 0.5C, 1C, 2C, 5C, 10C and recovering rate of 0.2C, respectively. The rGO@TiO₂ NFs showed 91% of initial capacity at 0.2C when the current density was reversed back to 0.2C, whereas the TiO₂ NFs exhibited 67% of initial capacity under same condition. The rGO@TiO₂ NFs clearly show significantly improved rate performances compared to those of the TiO₂ NFs at all rates. The higher reversible capacities and better cycle performances are evidences that wrapped graphene sheets significantly increase the electrical conductivity of TiO₂ NFs and offer higher electrode conductivity levels with their three-dimensionally interconnecting nanofibers in a complementary manner.

In summary, TiO₂ NFs with a wrinkled surface and a uniform diameter (200–300 nm) were synthesized via an electrospinning method. To improve the electrical conductivity of the TiO₂ NFs, rGO sheets were effectively wrapped onto PAH-grafted TiO₂ NFs. We verified that the sodiation mechanism is clearly based on an insertion process by conducting *ex-situ* XRD and *ex-situ* TEM analyses. The Na anode electrode with rGO@TiO₂ NFs delivered a high reversible capacity of 217 mAh g⁻¹ at 0.2C, excellent cycle performance at 1C (90% capacity retention during 200 cycles) and superior rate capability of 124 mAh g⁻¹ at a 5C rate (1.675 A g⁻¹). The graphene-wrapping assisted by the surface grafting of the TiO₂ NFs offers a versatile way to improve the electrical conductivity and electrochemical stability of TiO₂ NFs for application to Na ion batteries.

Methods

Materials. The titanium (iv) isopropoxide ($C_{12}H_{28}O_4Ti$, 98%), polyvinylpyrrolidone (PVP, $M_w = 1,300,000$), dimethylformamide (DMF, anhydrous, 99.8%), GO solution (2 ml mg^{-1}) and Poly(allylamine hydrochloride) (PAH, $M_w = 900,000$) were purchased from Sigma-Aldrich. Acetic acid (CH_3COOH , 99.9% (m/m)) was purchased from Junsei. We used all materials without further purification.

Synthesis of TiO_2 nanofibers. In a typical process, TiO_2 NFs were fabricated via electrospinning. First, 2g of titanium (iv) isopropoxide and 1g of acetic acid, as a precursor and a dissolving catalyst, respectively, were dissolved in 7g of DMF. Then, 1.2g of PVP as a sacrificial template was added to the solution. After stirring the precursor solution at 500 rpm for 12h, the solution was sequentially loaded into a plastic syringe. Under a voltage of 17kV and a flow rate of 0.3 mL min^{-1} , as-spun Ti precursor/PVP composite NFs were obtained. Here, the feeding rate of the solution was $10\mu\text{m/min}$, and a 25-gauge needle was used in the electrospinning condition. Finally, to decompose the matrix polymers and obtain TiO_2 NFs, the collected as-spun nanofibers were heat-treated at 500°C for 1h to decompose the matrix polymer and crystallize the TiO_2 NFs.

PAH functionalization and graphene-wrapping. $rGO@TiO_2$ NFs were synthesized by the following three methods. First, 1g of PAH was dissolved into 25ml of DI water, and an amount of 0.13g of TiO_2 NFs was added to this aqueous solution. This solution was mildly stirred for 1h to functionalize the surface of the TiO_2 NFs homogeneously into an amine end group. Then, centrifuging, washing and vacuum drying at 80°C for 6h followed. Second, an amount of 0.11g of prepared PAH- TiO_2 NFs was dispersed in 10ml of DI water, and $3200\mu\text{L}$ of aqueous GO solution was added to this mixture to synthesize GO-coated TiO_2 NFs as a hybrid anode material. Third, the GO-wrapped TiO_2 NFs were dispersed in 10ml of DI water, and 1.5g of hydrazine monohydrate was added to this solution to obtain $rGO@TiO_2$ NFs by reducing GO to rGO.

Material characterization. The anatase structure of TiO_2 was investigated by X-ray diffraction (XRD, D/MAX-RB (12KW) and D/MAX-RC (12kW), Rigaku). The morphologies of the TiO_2 NFs and $rGO@TiO_2$ NFs were observed by a scanning electron microscope (SEM, Philips). The lattice fringe and selected-area electron diffraction (SAED) patterns were obtained by a transmission electron microscope (TEM, Tecnai F30 S-Twin, FEI). Raman spectroscopy was carried out using a LabRAM HR UV/Vis/NIR PL device by Horiba Jobin Yvon, France. The Fourier-transform infrared spectroscopy (FT-IR) analysis was performed using the attenuated total reflection (ATR) method for the GO solution and the KBr-pellet method for the TiO_2 NFs and the $rGO@TiO_2$ NFs in transmission mode on an IFS66V/S & Hyperion 3000, Bruker Optiks, Germany. Carbon contents were measured by an element analysis (EA, Flash 2000 series, Thermo Scientific).

Electrochemical measurements. The composition of the slurries was 75 wt% active materials, 15 wt% Super P, and 10 wt% polyvinylidene fluoride (PVDF) binder dissolved in N-methyl-2-pyrrolidinone (NMP). The loading of the active material was about 0.85 mg cm^{-2} . Using a doctor blade technique, the slurry was coated onto Cu foils to a thickness of $90\mu\text{m}$. Then, overnight vacuum drying at 80°C followed. Celgard 2032 coin cells were used to assemble half-cells in an argon-filled glove box. To assemble the half-cells of NIBs, Na foils were used as the counter electrodes. Glass microfiber filters (Whatman) were used as the separator. The electrolyte was 1M of $NaClO_4$ in PC including 5 wt% of fluoroethylene carbonate (FEC). To prepare the half-cells for the LIBs, Li foils and Celgard 2400 were used as counter electrodes and as a separator, respectively. The electrolyte was 1M $LiPF_6$ in EC/DEC (1:1 v/v). Cell tests were carried out with a Maccor 4000 battery tester at a voltage window of $0.01\text{ V} \sim 2.5\text{ V}$. Cyclic voltammetry (CV) was performed on a WBCS3000 device by WonATech at a scan rate of 0.5 mV s^{-1} at $0.01\text{ V} \sim 2.5\text{ V}$.

References

- Palomares, V., Casas-Cabanas, M., Castillo-Martínez, E., Han, M. H. & Rojo, T. Update on Na-based battery materials. A growing research path. *Energy Environ. Sci.* **6**, 2312–2337 (2013).
- Slater, M. D., Kim, D., Lee, E. & Johnson, C. S. Sodium-Ion Batteries. *Adv. Funct. Mater.* **23**, 947–958 (2013).
- Yabuuchi, N., Kubota, K., Dahbi, M. & Komaba, S. Research Development on Sodium-Ion Batteries. *Chem. Rev.* **114**, 11636–11682 (2014).
- Ponrouch, A., Marchante, E., Courty, M., Tarascon, J.-M. & Palacin, M. R. In search of an optimized electrolyte for Na-ion batteries. *Energy Environ. Sci.* **5**, 8572–8583 (2012).
- Han, X., Li, T. & Hu, L. Tin Anode for Sodium-Ion Batteries Using Natural Wood Fiber as a Mechanical Buffer and Electrolyte Reservoir. *Nano Lett.* **13**, 3093–3100 (2013).
- Wang, J. W., Liu, X. H., Mao, S. X. & Huang, J. Y. Microstructural Evolution of Tin Nanoparticles during *In Situ* Sodium Insertion and Extraction. *Nano Lett.* **12**, 5897–5902 (2012).
- Darwiche, A. *et al.* Better Cycling Performances of Bulk Sb in Na-Ion Batteries Compared to Li-Ion Systems: An Unexpected Electrochemical Mechanism. *J. Am. Chem. Soc.* **134**, 20805–20811 (2012).
- Kim, Y. *et al.* An Amorphous Red Phosphorus/Carbon Composite as a Promising Anode Material for Sodium Ion Batteries. *Adv. Mater.* **25**, 3045–3049 (2013).
- Li, W. *et al.* $Sn_{4+x}P_3$ amorphous Sn-P composites as anodes for sodium-ion batteries with low cost, high capacity, long life, and superior rate capability. *Adv. Mater.* **26**, 4037–4042 (2014).
- Dahbi, M., Yabuuchi, N., Kubota, K., Tokiwa, K. & Komaba, S. Negative electrodes for Na-ion batteries. *Phys. Chem. Chem. Phys.* **16**, 15007–15028 (2014).

11. Xiao, L. *et al.* High capacity, reversible alloying reactions in SnSb/C nanocomposites for Na-ion battery applications. *Chem. Commun.* **48**, 3321–3323 (2012).
12. Xu, Y. *et al.* Nanocrystalline anatase TiO₂: a new anode material for rechargeable sodium ion batteries. *Chem. Commun.* **49**, 8973–8975 (2013).
13. Wu, L., Buchholz, D., Bresser, D., Gomes Chagas, L. & Passerini, S. Anatase TiO₂ nanoparticles for high power sodium-ion anodes. *J. Power Sources* **251**, 379–385 (2014).
14. González, J. R., Alcántara, R., Nacimiento, F., Ortiz, G. F. & Tirado, J. L. Microstructure of the epitaxial film of anatase nanotubes obtained at high voltage and the mechanism of its electrochemical reaction with sodium. *Cryst Eng Comm* **16**, 4602–4609 (2014).
15. Wu, L. *et al.* Unfolding the Mechanism of Sodium Insertion in Anatase TiO₂ Nanoparticles. *Adv. Energy Mater.* **5**, 1–11 (2014).
16. Hanaor, D. A. H. & Sorrell, C. C. Review of the anatase to rutile phase transformation. *J. Mater. Sci.* **46**, 855–874 (2011).
17. Su, X. *et al.* Advanced titania nanostructures and composites for lithium ion battery. *J. Mater. Sci.* **47**, 2519–2534 (2012).
18. Kim, J. & Cho, J. Rate Characteristics of Anatase TiO₂ Nanotubes and Nanorods for Lithium Battery Anode Materials at Room Temperature. *J. Electrochem. Soc.* **154**, A542–A546 (2007).
19. Wu, Q. L. *et al.* Aligned TiO₂ Nanotube Arrays As Durable Lithium-Ion Battery Negative Electrodes. *J. Phys. Chem. C* **116**, 18669–18677 (2012).
20. Wang, B. *et al.* Mesoporous CNT@TiO₂-C Nanocable with Extremely Durable High Rate Capability for Lithium-Ion Battery Anodes. *Sci. Rep.* **4**, 3729 (2014).
21. Cha, H. A., Jeong, H. M. & Kang, J. K. Nitrogen-doped open pore channeled graphene facilitating electrochemical performance of TiO₂ nanoparticles as an anode material for sodium ion batteries. *J. Mater. Chem. A* **2**, 5182–5186 (2014).
22. Ding, S. *et al.* Graphene-supported anatase TiO₂ nanosheets for fast lithium storage. *Chem. Commun.* **47**, 5780–5782 (2011).
23. Yang, S., Feng, X. & Müllen, K. Sandwich-Like, Graphene-Based Titania Nanosheets with High Surface Area for Fast Lithium Storage. *Adv. Mater.* **23**, 3575–3579 (2011).
24. Qiu, Y. *et al.* Synthesis of Size-Tunable Anatase TiO₂ Nanospindles and their Assembly into Anatase@Titanium Oxynitride/Titanium Nitride-Graphene Nanocomposites for Rechargeable Lithium Ion Batteries with High Cycling Performance. *ACS Nano* **4**, 6515–6526 (2010).
25. Li, N. *et al.* Battery Performance and Photocatalytic Activity of Mesoporous Anatase TiO₂ Nanospheres/Graphene Composites by Template-Free Self-Assembly. *Adv. Funct. Mater.* **21**, 1717–1722 (2011).
26. Chen, J. S., Wang, Z., Dong, X. C., Chen, P. & Lou, X. W. D. Graphene-wrapped TiO₂ hollow structures with enhanced lithium storage capabilities. *Nanoscale* **3**, 2158–2161 (2011).
27. Bruce, P. G., Scrosati, B. & Tarascon, J.-M. Nanomaterials for Rechargeable Lithium Batteries. *Angew. Chem. Int. Ed. Engl.* **47**, 2930–2946 (2008).
28. Satti, A., Larpent, P. & Gun'ko, Y. Improvement of mechanical properties of graphene oxide/poly(allylamine) composites by chemical crosslinking. *Carbon* **48**, 3376–3381 (2010).
29. Shin, J., Park, K., Ryu, W.-H., Jung, J.-W. & Kim, I.-D. Graphene wrapping as a protective clamping layer anchored to carbon nanofibers encapsulating Si nanoparticles for a Li-ion battery anode. *Nanoscale* **6**, 12718–12726 (2014).
30. Zhang, W. F., He, Y. L., Zhang, M. S., Yin, Z. & Chen, Q. Raman scattering study on anatase TiO₂ nanocrystals. *J. Phys. D: Appl. Phys.* **33**, 912–916 (2000).
31. Guo, H.-L., Wang, X.-F., Qian, Q.-Y., Wang, F.-B. & Xia, X.-H. A Green Approach to the Synthesis of Graphene Nanosheets. *ACS Nano* **3**, 2653–2659 (2009).
32. Goh, G. K. L., Han, X. Q., Liew, C. P. K. & Tay, C. S. S. Crystallinity and Orientation of Solution Deposited Anatase TiO₂ Films. *J. Electrochem. Soc.* **152**, C532–C536 (2005).
33. Wu, L., Buchholz, D., Bresser, D., Chagas, L. G. & Passerini, S. Anatase TiO₂ nanoparticles for high power sodium-ion anodes. *J. Power Sources* **251**, 379–385 (2014).
34. Koudriachova, M., Harrison, N. & de Leeuw, S. Orthorhombic Distortion on Li intercalation in Anatase. *Phys. Rev. B* **69**, 1–6 (2004).
35. Sudant, G., Baudrin, E., Larcher, D. & Tarascon, J.-M. Electrochemical lithium reactivity with nanotextured anatase-type TiO₂. *J. Mater. Chem.* **15**, 1263–1269 (2005).
36. Kim, K. T. *et al.* Anatase Titania Nanorods as an Intercalation Anode Material for Rechargeable Sodium Batteries. *Nano Lett.* **14**, 416–422 (2014).

Acknowledgements

This work was supported by a grant from the Korea CCS R&D Center (KCRC) funded by the Korean government (Ministry of Science, ICT & Future Planning) (No. NRF-2014M1A8A1049303).

Author Contributions

Y.Y. and J.W.J. contributed to conceiving the concept. Y.Y. established nearly all parts of the experimental system and carried out the measurements and characterizations, and J.W.J. assisted with some parts. Y.Y., J.W.J. and K.P. wrote the text of the entire manuscript and prepared all figures together. J.W.J. drew the Fig. 1. K.P. provided research advice, and I.D.K. oversaw the project and led the effort to completion. All authors reviewed the manuscript.

Additional Information

Supplementary information accompanies this paper at <http://www.nature.com/srep>

Competing financial interests: The authors declare no competing financial interests.

How to cite this article: Yeo, Y. *et al.* Graphene-Wrapped Anatase TiO₂ Nanofibers as High-Rate and Long-Cycle-Life Anode Material for Sodium Ion Batteries. *Sci. Rep.* **5**, 13862; doi: 10.1038/srep13862 (2015).



This work is licensed under a Creative Commons Attribution 4.0 International License. The images or other third party material in this article are included in the article's Creative Commons license, unless indicated otherwise in the credit line; if the material is not included under the Creative Commons license, users will need to obtain permission from the license holder to reproduce the material. To view a copy of this license, visit <http://creativecommons.org/licenses/by/4.0/>